

The stellar-to-halo mass relation of central galaxies across three orders of halo mass

Victoria Toptun^{1*}, Paola Popesso^{1,2}, Ilaria Marini^{2,1}, Stephan Vladutescu-Zopp¹, Klaus Dolag^{3,4,2}, Peter Behroozi⁵, Lorenzo Lovisari^{6,7}, Stefano Ettori^{8,9}, Veronica Biffi^{10,11}, Xiaohu Yang^{12,13}, Natanael de Isidio¹, and Daudi T. Mazengo^{1,14}

¹ European Southern Observatory, Karl Schwarzschildstrasse 2, 85748, Garching bei München, Germany

² Excellence Cluster ORIGINS, Boltzmannstr. 2, D-85748 Garching bei München, Germany

³ Universitäts-Sternwarte, Fakultät für Physik, Ludwig-Maximilians-Universität München, Scheinerstr.1, 81679 München, Germany

⁴ Max-Planck-Institut für Astrophysik, Karl-Schwarzschildstr. 1, 85741 Garching bei München, Germany

⁵ Department of Astronomy and Steward Observatory, University of Arizona, Tucson, AZ 85721, USA

⁶ INAF, Istituto di Astrofisica Spaziale e Fisica Cosmica di Milano, via A. Corti 12, 20133 Milano, Italy

⁷ Center for Astrophysics | Harvard & Smithsonian, 60 Garden Street, Cambridge, MA 02138, USA

⁸ INAF, Osservatorio di Astrofisica e Scienza dello Spazio, via Piero Gobetti 93/3, 40129 Bologna, Italy

⁹ INFN, Sezione di Bologna, viale Berti Pichat 6/2, 40127 Bologna, Italy

¹⁰ INAF, Osservatorio Astronomico di Trieste, Via Tiepolo 11, 34143 Trieste, Italy

¹¹ IFPU, Institute for Fundamental Physics of the Universe, Via Beirut 2, I-34014 Trieste, Italy

¹² State Key Laboratory of Dark Matter Physics, Tsung-Dao Lee Institute & School of Physics and Astronomy, Shanghai Jiao Tong University, Shanghai 201210, China

¹³ Shanghai Key Laboratory for Particle Physics and Cosmology, and Key Laboratory for Particle Physics, Astrophysics and Cosmology, Ministry of Education, Shanghai Jiao Tong University, Shanghai 200240, China

¹⁴ Physics Department, College of Natural and Mathematical Sciences, P.O.Box 338, The University of Dodoma, Tanzania

Received ; accepted

ABSTRACT

The stellar content of galaxies is tightly connected to the mass and growth of their host dark matter halos. Observational constraints on this relation remain limited, particularly for low-mass groups, leaving uncertainties in how galaxies assemble their stars across halo mass scales. Accurately measuring the brightest central galaxy (BCG) stellar-to-halo mass relation (SHMR) over a wide mass range is therefore crucial for understanding galaxy formation and the role of feedback processes. Here we present the SHMR spanning $M_{\text{halo}} \sim 10^{12} \text{--} 10^{15} M_{\odot}$, using halo masses derived from eROSITA eRASS1 X-ray data and BCG stellar masses based on SDSS photometry. By stacking X-ray spectra of optically selected groups, we recover robust average halo gas temperatures for each bin, which are then converted to halo masses via the M - T_X relation. We find that the SHMR peaks near $M_{\text{halo}} \sim 10^{12} M_{\odot}$, with a declining stellar fraction at higher masses. This trend reflects a combination of processes that reduce the efficiency of stellar mass growth in massive halos, such as AGN feedback, reduced cooling efficiency, and the increasing dominance of ex-situ assembly, while halos continue to grow through mergers and accretion. Our measurements are consistent over the full mass range with previous observational studies, including weak lensing, X-ray analyses of individual clusters, and kinematical and dynamical methods. Comparisons with hydrodynamical simulations show good agreement at low masses but reveal significant discrepancies in the normalization at cluster scales, highlighting the sensitivity of BCG stellar growth to feedback prescriptions and halo assembly history. These results provide the first X-ray-based observational SHMR covering three orders of magnitude in halo mass, establish a robust benchmark for testing galaxy formation models.

Key words. Galaxies: groups: general - X-rays: general - X-rays: galaxies: clusters - galaxies: active - methods: data analysis

1. Introduction

Galaxy formation is fundamentally linked to the growth of dark matter halos, creating a strong correlation between galaxy properties, especially stellar mass, and the mass and gravitational potential of their host halos (Conroy & Wechsler 2009; Behroozi et al. 2010; Moster et al. 2010). Central galaxies, which reside at the centers of these halos, are particularly shaped by the mass and structure of their hosts. While most galaxies live in relatively small halos, within the galaxy group regime, that contain the bulk of the universe's baryonic matter (98% of systems; Yang

et al. 2007; Robotham et al. 2011; Popesso et al. 2024a), the majority of studies on halo-driven galaxy evolution have focused on the small minority that reside in massive galaxy clusters above $M_{\text{halo}} \sim 10^{14} M_{\odot}$. In this work, we extend the scope of such studies for the first time across three orders of magnitude in halo mass, targeting group-scale systems down to halos comparable in mass to that of the Milky Way.

A central example of the galaxy-halo connection is the stellar-to-halo mass relation (SHMR), which quantifies how the stellar mass of central galaxies scales with the total mass of their dark matter halos. Semi-empirical models show that the stellar-to-halo mass ratio for central galaxies increases steeply from

* victoria.toptun@eso.org

low-mass halos, which host dwarf systems, up to a peak near $M_{500} \sim 10^{12}\text{--}10^{12.5} M_{\odot}$, characteristic of halos similar in mass to the Local Group. Beyond this scale, the ratio declines with increasing halo mass, indicating that the efficiency of converting baryons into stars drops sharply in more massive halos and becomes very low in systems like massive galaxy clusters (Moster et al. 2013, 2018; Lu et al. 2015; Rodríguez-Puebla et al. 2017; Behroozi et al. 2013; Birrer et al. 2014; Behroozi et al. 2019).

This characteristic shape of the SHMR captures how stellar mass assembly in central galaxies is regulated by the shifting balance of feedback processes across halo mass scales. In low-mass halos below $M_{\text{halo}} \sim 10^{12} M_{\odot}$, typically hosting a single central galaxy, supernova-driven winds and stellar feedback dominate but lose effectiveness as halo mass increases and the gravitational potential deepens. At this stage, gas accretion is still insufficient to trigger efficient active galactic nucleus (AGN) activity (de Isidro et al. 2024; Mancera Piña et al. 2025). In higher mass halos above $M_{\text{halo}} \sim 10^{13} M_{\odot}$, AGN feedback becomes the dominant quenching mechanism, suppressing further star formation (Kravtsov et al. 2018; Erfanianfar et al. 2019; Golden-Marx et al. 2022) with long gas cooling times further limiting the supply of cold gas. Around the peak mass, where stellar and AGN feedback are comparably effective, halos reach their maximum efficiency in converting baryons into stars.

The AGN feedback is likely not the only process shaping this trend. Decreasing gas cooling efficiency in massive halos, the increasing importance of ex-situ (merger-driven) stellar mass assembly, and halo assembly bias can all contribute to the observed behavior of the SHMR. The presence of the SHMR peak cannot be explained solely by AGN-driven gas depletion and the associated decrease in M_{halo} : gas fractions in systems with $M_{\text{halo}} \sim 10^{13} M_{\odot}$ are typically $\sim 3\%$ (Pratt et al. 2009; Eckert et al. 2016; Popesso et al. 2024b) and can reach the universal baryon fraction ($\Omega_b/\Omega_m = 0.154$, Planck Collaboration et al. 2020) in massive clusters, which is insufficient to account for the more than order-of-magnitude variation observed in the SHMR. Moreover, the shape of the SHMR reflects the cumulative influence on the BCG across the history of the system, rather than the instantaneous state of the present epoch. This is the reason why the SHMR is considered a fundamental relation in galaxy evolution.

Nevertheless, the SHMR remains only partially constrained, primarily due to the difficulty of accurately measuring halo masses. While stellar masses are available for large galaxy samples in surveys such as SDSS, DESI, and GAMA, precise and consistent halo mass estimates are typically limited to the most massive systems, galaxy clusters, where reliable mass proxies exist, but which represent only a small fraction of the population.

Weak gravitational lensing (WL) directly probes the total projected mass distribution through the distortion of background galaxies. It has been widely applied to constrain the SHMR over a broad range of halo masses, from galaxies to massive clusters (Mandelbaum et al. 2006, 2016; Hoekstra et al. 2005; Reyes et al. 2012; Hudson et al. 2015; van Uitert et al. 2011, 2016; Dvornik et al. 2020; Wang et al. 2022). The primary advantage of WL is that it is independent of baryonic tracers, although it requires deep, wide-field imaging and careful control of systematic effects, including shear calibration and accurate source redshift estimation.

Indirect halo mass estimates rely on observables correlated with halo mass, such as richness, magnitude gap, or velocity dispersion, calibrated against external measurements (Golden-Marx & Miller 2019; Golden-Marx et al. 2022; Hansen et al.

2009; More et al. 2011; van der Burg et al. 2014; Golden-Marx & Miller 2018). These methods cover groups to massive clusters ($M_{\text{halo}} \sim 10^{13}\text{--}10^{15} M_{\odot}$). However, they have large intrinsic scatter and require external calibration, making them indirectly dependent on stellar mass.

Semi-analytical approaches, such as abundance matching and empirical modeling, connect galaxies to halos statistically by matching observed stellar mass or luminosity functions to simulated halo mass functions (Yang et al. 2009; Conroy & Wechsler 2009; Guo et al. 2010; Moster et al. 2010, 2013, 2018; Behroozi et al. 2010, 2013, 2019; Reddick et al. 2013; Shankar et al. 2017; Rodríguez-Puebla et al. 2017; Yang et al. 2012). These models span the entire halo mass range ($M_{\text{halo}} \sim 10^9\text{--}10^{15} M_{\odot}$) and can explore redshift evolution. By construction, however, they are indirect, rely on assumptions regarding scatter and star formation efficiency, and may be biased toward certain galaxy populations, such as red or quenched systems.

X-ray observations of the hot intracluster and intragroup medium provide an alternative route to direct halo mass estimation. Indeed, the temperature of the hot gas is considered a very accurate proxy of the halo mass in virialized systems due to the predicted and observed tight correlation between temperature and mass (Lin & Mohr 2004; Gonzalez et al. 2013; Kravtsov et al. 2018; Erfanianfar et al. 2019; Chiu et al. 2016, 2025; Akino et al. 2022; DeMaio et al. 2018). This approach is robust for massive halos ($M_{\text{halo}} \gtrsim 10^{14} M_{\odot}$), where the hot gas dominates, but becomes increasingly limited in lower-mass systems, where X-ray emission is generally too faint for reliable measurements of individual halos for the most of the sample. Indeed, detecting low-mass halos ($10^{12} < M_{\text{halo}} < 10^{14} M_{\odot}$) in X-rays remains challenging. As a result, obtaining reliable halo mass estimates from X-ray observations is difficult for most low-mass groups on an individual basis.

Stacking offers a powerful method to overcome the limitations in measuring individual halo properties. By combining X-ray spectra from galaxy groups selected through different techniques, it becomes possible to recover average gas temperatures and total X-ray luminosity (Toptun et al. 2025; Zheng et al. 2023). Wide-field surveys such as the eROSITA All-Sky Survey (eRASS1; Merloni et al. 2024) and the upcoming eRASS:4 do not provide complete samples of galaxy groups across large volumes, due to strong selection effects (Popesso et al. 2024a, 2025b; Marini et al. 2024). However, these surveys enable the stacking of large numbers of faint systems, significantly boosting the signal-to-noise ratio and allowing the study of group-scale halos that are too faint to detect individually.

In this paper, we use spectral stacking to measure gas temperatures and infer halo masses across more than three decades in halo mass. This approach allows us, for the first time, to observationally trace the SHMR down to $M_{\text{halo}} \approx 10^{12} M_{\odot}$, with stellar and halo masses independently derived from optical and X-ray data, respectively. In contrast to previous studies, which focused on limited mass ranges or required individually detected systems, we present average measurements for a large, optically selected population of galaxy groups spanning a broad range in halo mass. The efficiency, completeness, and purity of the optical group catalog used as a parent sample (Yang et al. 2007) have been extensively validated in previous works (Popesso et al. 2025b; Marini et al. 2024, 2025a,b). We stack this group sample using data from eRASS1 to provide the first observational constraints on the SHMR from Milky Way-mass galaxy groups up to massive clusters.

Throughout this paper, we adopt a flat Λ CDM cosmology with $\Omega_m = 0.27$ and $H_0 = 70 \text{ km s}^{-1} \text{ Mpc}^{-1}$, and used Chabrier

IMF (Chabrier 2003). R_Δ is the radius within which the mean density of the halo is Δ times higher than the critical density of the Universe, and M_Δ is the total mass enclosed within this radius.

2. Analysis framework

2.1. Identifying halos and their central galaxy

Galaxy groups were selected from the catalog of Yang et al. (2007), covering the low-redshift range up to $z < 0.2$. The reliability of this optical selection algorithm in identifying galaxy groups and their central galaxies was assessed by Marini et al. (2024), who compared its performance against a simulated galaxy lightcone based on the MAGNETICUM¹ (Dolag et al. 2016, 2025) simulation. The algorithm presented in Yang et al. (2007) achieves a 95% completeness in the reconstruction of the simulated sample down to $\sim 10^{12} M_\odot$, with high purity ($> 93\%$). Moreover, the identification of central galaxies is highly efficient, with a success rate of 97%. The resulting halo mass proxy is accurate enough to allow binning by halo mass with minimal contamination from systems of lower or higher mass, as quantified in Popesso et al. (2025b). Previous analysis of the skewness and kurtosis of a similar sample indicates that, on average, the systems tend to be virialized (Popesso et al. 2025a).

We followed the methodology of Toptun et al. (2025) for group selection, X-ray data extraction, and spectral stacking. We expanded the sample to include systems with either a brightest central galaxy (BCG) stellar mass of $M_{*,\text{BCG}} > 10^{10.3} M_\odot$, using stellar masses from GSWLC-X2 catalog (Salim et al. 2016), and a halo mass of $M_{200} > 10^{11.7} M_\odot$, estimated from characteristic luminosities via a mass-to-light ratio in the Yang et al. (2007) catalog. These selection criteria increased the sample size to 118,058 systems with halo masses below $10^{14} M_\odot$.

While the high performance of the Yang et al. (2007) group finder is confirmed for systems with $M_{200} < 10^{14} M_\odot$, as discussed above, its purity and completeness at the high-mass end, on cluster scales, may be affected by fragmentation (Marini et al. 2024). To mitigate this effect, we constructed the high-mass end of the sample ($M_{200} > 10^{14} M_\odot$) by cross-matching the Yang et al. (2007) catalog with the eRASS1 X-ray-selected cluster catalog, resulting in a sample of 689 clusters. Since clusters in this mass range are expected to be sufficiently X-ray luminous to be detected in eRASS1 (Popesso et al. 2024a), this approach is not expected to introduce significant selection biases.

For each group, source and background X-ray spectra were extracted from the eRASS1 public event lists. Source spectra were measured within R_{500} , centered on the BCG coordinates, while background spectra were extracted from annular regions spanning 1.5–1.8 R_{500} , with the annulus area matched to the area of the source region to ensure consistent background subtraction.

To test the robustness of the results against intrinsic scatter and measurement uncertainties, we perform the stacking analysis using two independent binning schemes: one based on BCG stellar mass and the other based on the optical halo mass proxy. This bidirectional binning approach allows us to assess the robustness of the derived $M_{*,\text{BCG}}-T_X$, and thus of the $M_{*,\text{BCG}}-M_{\text{halo}}$ relation and to test for potential biases introduced by binning along a single axis. By comparing the resulting relations, we can verify the consistency of the observed trends, independent of the choice of binning variable.

The spectra in each bin were stacked to produce an average spectrum representative of that mass range. After stacking, the background spectra were subtracted from the corresponding source-plus-background spectra before spectral modeling. As demonstrated in Toptun et al. (2025), this background-subtraction approach gives consistent results with those obtained from the simultaneous modeling of the source-plus-background and background spectra. Bin definitions and the corresponding stacked background-subtracted spectra are provided in the Appendix A. Additional details on the selection process, data extraction, stacking procedure, and validation tests can be found in Toptun et al. (2025).

2.2. Deriving gas temperatures and halo masses

We fitted the stacked spectra in each bin using the Sherpa (v4.17.0) Python package (Burke et al. 2023), modeling the emission with multiple components: an intracluster medium (ICM) component, a power-law component representing unresolved AGN, and Galactic line-of-sight absorption. Since the XRB contribution is low (Toptun et al. 2025) and has a similar power-law shape that may lie within the error budget of the AGN component, we do not model it separately.

The ICM emission was described using the GADEM² model, which represents a multi-temperature plasma with a Gaussian distribution of emission measure, implemented as a combination of multiple MEKAL³ components (Mewe et al. 1985, 1986; Liedahl et al. 1995). For each bin, the initial predictions of the mean temperature and Gaussian width were derived from the predicted temperature distribution of the halos in that bin, based on the mass-temperature relation of Toptun et al. 2025 and halo masses from the Yang et al. 2007 group catalog. During the fitting process, the mean temperature was allowed to vary, while the width of the temperature distribution was fixed to reduce the number of free parameters and to limit degeneracies in the fit. Allowing the width to vary increases the statistical uncertainties and introduces degeneracies or spurious local minima, without significantly changing the best-fit width. For this reason, we fixed the width to ensure a more robust fit (see Figure A.2 for a comparison). Following the recommendations of Baumgartner et al. (2003); Gastaldello et al. (2021); Ghizzardi et al. (2021); Urban et al. (2017), the metal abundance in each bin was fixed to $0.3 Z_\odot$ using the abundance table from Anders & Grevesse (1989). For more details on the impact of different metal abundance assumptions, see Section 4.3.

The power-law component accounts for unresolved AGN, which are particularly important in the low-mass bins (see also Popesso et al. 2025b; Toptun et al. 2025). To limit the number of free parameters, the photon index was fixed to the average AGN value $\Gamma = 1.95$ (Nandra & Pounds 1994). Because the stacked spectra, especially at low halo masses, have limited signal-to-noise, leaving both the ICM and AGN normalizations free can lead to degeneracies between the fitted parameters. We therefore constrained the relative normalization of the two components using the ICM-to-AGN flux ratio predicted by the MAGNETICUM hydrodynamical simulation (Toptun et al. 2025). This ratio is a function of halo mass. Since M_{500} is not known a priori and is instead inferred from the fitted temperature through the $M-T_X$ relation, the normalization constraint was implemented

² <https://heasarc.gsfc.nasa.gov/xanadu/xspec/manual/XSmodelGadem.html>

³ <https://heasarc.gsfc.nasa.gov/docs/xanadu/xspec/manual/XSmodelMekal.html>

¹ <http://www.magneticum.org/index.html>

as a temperature-dependent relation. During the fitting process, for each temperature iteration, the corresponding halo mass was computed, and the ICM-to-AGN normalization ratio was updated accordingly. The ICM component dominates in the regions of the Fe-L and Fe-K complexes, while the power-law contributes primarily at the edges of the eROSITA effective area (below ~ 0.5 keV and above ~ 1.5 keV). Line-of-sight absorption was included, with initial n_{H} values taken from the FTOOLS database and allowed to vary with lower/upper bounds of $0.1 - 0.7 \cdot 10^{22} \text{ cm}^{-2}$.

From the fitted spectra, we derived the average temperatures for each BCG-stellar- and halo- mass bin (see Appendix A) and converted them to X-ray-based halo masses, M_{500} , using the $M-T_X$ relation (Lovisari et al. 2015). Uncertainties on the temperature measurements and, consequently, on M_{500} were estimated via the bootstrap procedure described and validated in Toptun et al. (2025). M_{500} was then converted to M_{200} using the PYTHON package COLOSSUS (Diemer 2018). A comparison between the X-ray- and optically based halo mass estimates shows high consistency between the two, supporting the reliability of the mass measurements (see Appendix A.1). A comparison between the average temperature of individual spectra in the highest-mass bin and the corresponding stacked result is provided in Appendix B.

3. Linking BCG stellar mass and halo temperature

Figure 1 shows the stacked X-ray temperatures as a function of BCG stellar mass. The relation is presented for both stellar-mass and halo-mass binning; in the latter case, the binning is based on optically derived halo masses from Yang et al. (2007), and we plot the average stellar mass of the BCG within each sub-bin.

We recover well-defined temperatures across all bins, revealing a smooth, approximately log-linear increase of temperature with stellar mass, from $M_{\star,\text{BCG}} \approx 10^{10.3} M_{\odot}$ to $M_{\star,\text{BCG}} \approx 10^{11.8} M_{\odot}$. The results obtained from stellar-mass and halo-mass binning agree within the uncertainties, indicating that the choice of binning does not strongly affect the overall trend. However, as shown in the Appendix A, spectra corresponding to the halo-mass bins at the low-mass end exhibit fewer degrees of freedom and systematically higher χ^2 values in the spectral modeling. This likely reflects inaccuracy in the halo mass proxy either due to incompleteness in the group membership or in the calibration of the mass proxy.

The observed correlation confirms the expected connection between the stellar content of BCGs and the depth of the halo potential, providing a direct link between galaxy properties and halo properties. This result supports the use of the stellar mass of BCGs as a reliable proxy for halo mass across the group-to-cluster mass regime.

We fit the $M_{\star,\text{BCG}}-T_X$ relation using Orthogonal Distance Regression (ODR) implemented via the `scipy.odr` module from the `scipy` PYTHON package, accounting for uncertainties in the temperature axis. The best fit of the relation is obtained separately for the two binning schemes:

$$\log_{10}\left(\frac{T_X}{1 \text{ keV}}\right) = 1.28 \pm 0.13 \cdot \log_{10}\left(\frac{M_{\star,\text{BCG}}}{M_{\odot}}\right) - 14.43 \pm 1.47, \quad (1)$$

for M_{200} binning scheme, and

$$\log_{10}\left(\frac{T_X}{1 \text{ keV}}\right) = 1.05 \pm 0.15 \cdot \log_{10}\left(\frac{M_{\star,\text{BCG}}}{M_{\odot}}\right) - 11.82 \pm 1.61, \quad (2)$$

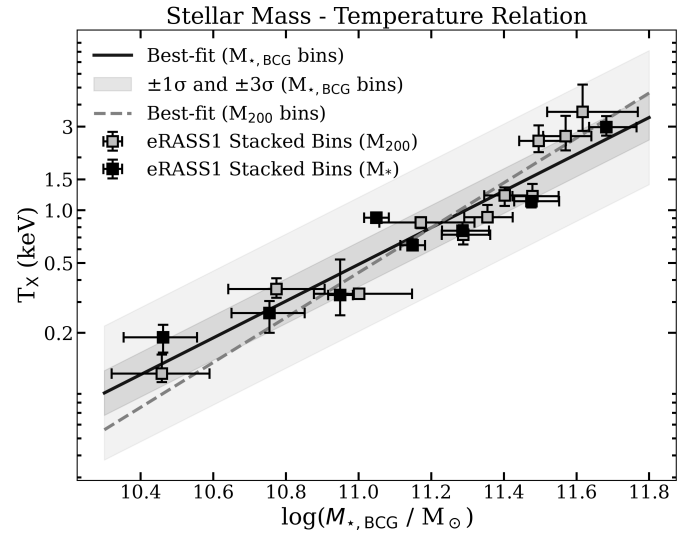


Fig. 1. Stacked X-ray temperatures within R_{500} as a function of BCG stellar mass. Black points correspond to bins defined by stellar mass, while grey points correspond to bins defined by optically based halo mass (Yang et al. 2007); for both binning schemes, the average BCG stellar mass of each sub-bin is plotted on the x-axis. Error bars on the y-axis indicate 1σ uncertainties derived from bootstrap resampling, while error bars on the x-axis represent the 1σ interval around the mean. Best-fit relations for both binning schemes are shown as black solid and grey dashed lines. The shaded area corresponds to the 1σ and 3σ uncertainties of the best-fit.

for M_{*} binning scheme.

Since the difference between the two fitted relations is minor (within 1.4σ), it confirms that both subsamples follow the same $M_{\star,\text{BCG}}-T_X$ trend and the observed relation is independent of the binning variable.

4. Stellar-to-halo mass relation

4.1. First observational view of the relation

Figure 2 presents the stellar-to-halo mass relation (SHMR) derived from the X-ray-based halo masses. Our measurements cover the range $M_{\text{halo}} \approx 10^{12}-10^{15} M_{\odot}$, providing the first observational SHMR spanning this full mass range with halo masses directly inferred from X-ray gas temperatures. Error bars indicate 1σ uncertainties derived via bootstrap resampling of the stacked spectra.

Around the expected characteristic turnover, we observe a plateau in the stellar-to-halo mass ratio, $M_{\star,\text{BCG}}/M_{\text{halo}}$, which remains approximately constant within the uncertainties. This feature indicates that the turnover is well captured in our data, corresponding to the peak in star formation efficiency near $M_{\text{halo}} \sim 10^{12} M_{\odot}$ (Yang et al. 2009; Conroy & Wechsler 2009; Behroozi et al. 2010; Guo et al. 2010). Above this halo mass, the ratio declines, reflecting the increasing importance of AGN feedback in suppressing in-situ star formation (Silk & Rees 1998; McNamara & Nulsen 2007; Kravtsov & Borgani 2012).

Extending the SHMR to lower halo masses to fully map the turnover and subsequent decline is currently unfeasible, even with deeper wide-field surveys such as eRASS:4. At $M_{\text{halo}} \approx 10^{11} M_{\odot}$, the expected X-ray temperature is $T_X = 0.036 \pm 0.009$ keV, corresponding to halos whose gas content is negligible. In this regime, the bulk of the emission lies outside the sensitive energy range of current X-ray observatories (eROSITA,

XMM-Newton, and Chandra), making direct detection and reliable spectral modeling impossible for such halos. For the same reason, we note that the temperatures in the lowest-mass bins should be interpreted with caution, as they lie close to the low-energy sensitivity limit, which may introduce additional systematic uncertainties.

As for the $M_{\star, \text{BCG}} - T_X$ relation, the stacked points from the two binning schemes show good agreement. To fit the SHMR, we select only the $M_{\star, \text{BCG}}$ binning, which provides smaller uncertainties on the derived temperatures (See Appendix A.1). The best fit of the relation is obtained with ODR in two ways. First, we simply fit a power law to the data at halo masses larger than the knee $M_{\text{peak}} \approx 4 \cdot 10^{12} M_{\odot}$. The best fit is:

$$\log_{10} \left(\frac{M_{\star, \text{BCG}}}{M_{200}} \right) = -0.69 \pm 0.05 \cdot \log_{10} \left(\frac{M_{200}}{M_{\odot}} \right) - 7.13 \pm 0.77, \quad (3)$$

Second, we fit the entire relation with a double power law following the prescription from Behroozi et al. (2019), but without a Gaussian component:

$$\log_{10} \left(\frac{M_{\star, \text{BCG}}}{M_0} \right) = \epsilon - \log_{10} \left(10^{-\alpha x} + 10^{-\beta x + \kappa} \right), \quad (4)$$

$$x = \log_{10} \left(\frac{M_{200}}{M_0} \right) \quad (5)$$

Here we are fixing the faint end slope $\alpha = 1.963$ and scale $\log_{10}(M_0/M_{\odot}) = 12.035$ following Behroozi et al. (2019) best-fit value and leaving free parameters constraining the bright end slope β and normalization ϵ . The best fit values are:

$$\begin{aligned} \beta &= 0.27 \pm 0.10, \\ \epsilon &= -1.59 \pm 0.09, \\ \kappa &= -0.45 \pm 0.19. \end{aligned}$$

Both best-fit relations are shown in Figure 2. While a single power law describes the data well over the fitted mass range, the double power law not only reproduces the data to the right of the knee, but also accurately captures the shape of the knee for the M_{\star} binning scheme.

4.2. Comparison with previous results

Figure 2 compares our SHMR measurements with a selection of literature results (not all studies are shown to preserve figure clarity; additional references are discussed in the text). For the comparison, we converted all the literature stellar masses to the Chabrier IMF (Chabrier 2003) if a different IMF were used. Overall, the results are consistent within uncertainties across various methods, despite significant scatter.

In earlier sections, we discussed how differences in halo mass estimation can impact the SHMR (see Section 1). However, variations in BCG stellar mass estimates also play a role. While all the literature data were converted to the same IMF, other assumptions, such as star formation history, dust, and metallicity, can also affect the stellar mass estimates and contribute to the scatter between studies.

Moreover, even among SED-based approaches with consistent model assumptions, the choice of spatial aperture for measuring stellar mass can significantly influence the resulting SHMR. We adopt the stellar masses from Salim et al. (2016),

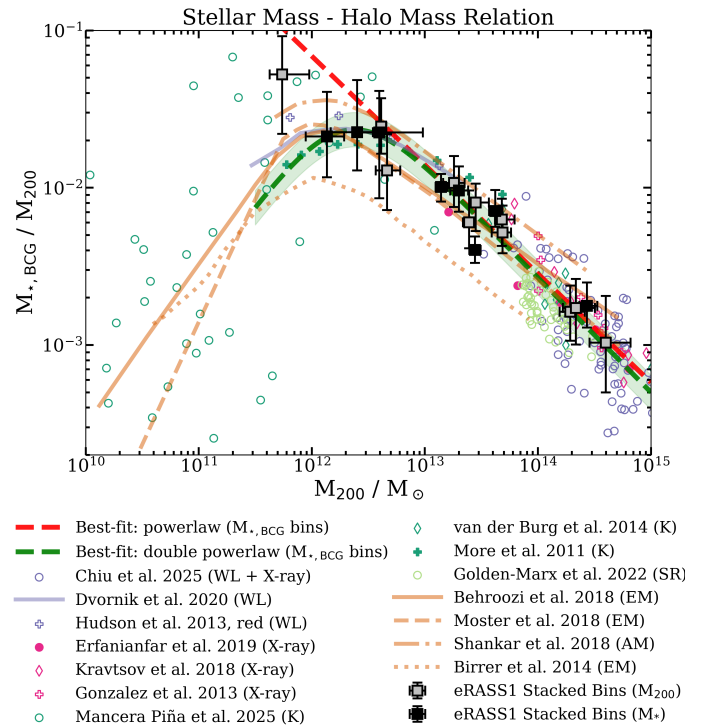


Fig. 2. BCG stellar-to-halo mass ratio as a function of halo mass. The meaning of the symbols is as in Figure 1. Best-fit relations are shown as green and red dashed lines; the shaded region indicates the 1σ uncertainty of the double power-law best-fit relation. Literature measurements are color-coded by halo mass estimation method as indicated in the legend: violet for weak lensing (WL), red for X-ray, green for kinematical and dynamical studies (K), and light green for scaling relations (SR); for the literature data, filled points indicate stacking results, while empty points show results for individual sources. Orange lines correspond to semi-analytical predictions from abundance matching (AM) and empirical modeling (EM).

which are derived using a broad range of photometric bands (from near-UV to far-infrared) and a PDF-matching method. In contrast, studies that rely on significantly larger apertures, which can include contributions from intracluster light (ICL), tend to produce flatter SHMR slopes at the high-mass end due to systematically higher BCG stellar masses at the cluster scale (Kravtsov et al. 2018; DeMaio et al. 2018). The ICL contribution may account for up to $\sim 25\%$ of the total stellar mass of cluster members (Montenegro-Taborda et al. 2025; Mayes et al. 2025). In this work, we do not explore the effect of larger apertures for galaxy groups. While ICL can measurably affect BCG stellar masses in clusters, its contribution at the group scale is expected to be smaller and remains poorly constrained, and we therefore do not include it in our analysis. To maintain consistency and avoid aperture-related biases, we base our SHMR on stellar masses that exclude intracluster and intragroup light, and compare only with measurements derived using similar apertures. Specifically, for the Kravtsov et al. 2018 data shown in Figure 2, we adopt the values measured within 50 kpc, following the approach of Chiu et al. 2025.

At the high-mass end, our results show excellent consistency with individual eRASS1 cluster detections from Chiu et al. (2025), which naturally align with the best-fit SHMR. Similar agreement is found with other studies based on X-ray-derived halo masses (Erfanianfar et al. 2019; Gonzalez et al. 2013; Kravtsov et al. 2018) and with halo mass estimates inferred from

optical scaling relations (van der Burg et al. 2014; Golden-Marx & Miller 2018).

At lower halo masses, we find good agreement with observational constraints on the location of the SHMR knee. In the vicinity of the knee and toward higher halo masses, the SHMR normalization reported by Dvornik et al. (2020), based on weak-lensing-calibrated halo masses in the GAMA survey area, is consistent with our results. Similar consistency is found in studies relying on optical mass proxies over more limited halo mass ranges, such as More et al. (2011). At the lowest halo masses probed in this study, closer to the regime of individual galaxy halos, our measurements connect smoothly to the high-mass end of the galactic-halo sample (Mancera Piña et al. 2025; Munshi et al. 2021; de Isidio et al. 2024).

Among semi-empirical models, most (Moster et al. 2010; Behroozi et al. 2013, 2019; Wang et al. 2013; Lu et al. 2015; Rodríguez-Puebla et al. 2017; Shankar et al. 2017) are consistent with our measurements within 1σ , with the exception of Birrer et al. (2014), which shows a moderate offset toward lower stellar-to-halo mass ratios.

4.3. Impact of gas metallicity

We explored the impact of the assumed gas-phase metal abundance in the spectral modeling on the derived stellar-to-halo mass relation (SHMR). In our main analysis, the metal abundance in each halo mass bin was fixed to a constant value of $0.3 Z_{\odot}$ (see Section 2.2). To assess the sensitivity of our results to this assumption, we performed an alternative analysis in which the metal abundance was allowed to vary with halo mass, adopting the mean metal abundance within R_{500} derived from the MAGNETICUM hydrodynamical simulation for each bin, since observationally the gas metallicity for the lowest mass bins is poorly constrained. The metal abundances were computed for the hot gas only, weighted by particle mass. Figure 3, lower panel, shows the resulting mean metal abundance as a function of halo mass, which was used for the spectral modeling in this comparison analysis.

Figure 3, upper panel, compares the SHMR obtained using the fixed metal abundance of $0.3 Z_{\odot}$ with the relation derived when adopting the MAGNETICUM-based metal abundance. At halo masses $\log(M_{\text{halo}}/M_{\odot}) > 13$, the SHMR is unchanged between the two assumptions. At lower halo masses, the metallicity inferred from the simulation leads to slightly higher stellar-to-halo mass ratios compared to the fixed-abundance case, although for the most bins the difference remains within the statistical uncertainties.

This behavior indicates that the lowest-mass bins, corresponding to a regime closer to individual galaxies than to clusters, are more sensitive to the assumed metal abundance in the spectral modeling. In contrast, the average temperatures of groups and clusters with $\log(M_{\text{halo}}/M_{\odot}) \gtrsim 13$ are not that sensitive to the choice of metallicity, consistent with previous findings (Toptun et al. 2025). For the lowest-mass bins, the predicted gas metallicity is around $0.6 Z_{\odot}$, which allows us to test how the SHMR changes across a physically expected range of metallicities. Higher metallicity shifts the peak of the star formation efficiency to lower halo masses ($\sim 3 \cdot 10^{11} M_{\odot}$) and increases the stellar-to-halo mass ratios. However, this also alters the shape of the SHMR: with this peak position, the low-mass side before the peak no longer aligns with observational constraints from individual galaxies based on kinematics (Mancera Piña et al. 2025; Munshi et al. 2021), supporting our choice of $0.3 Z_{\odot}$ as the fiducial abundance.

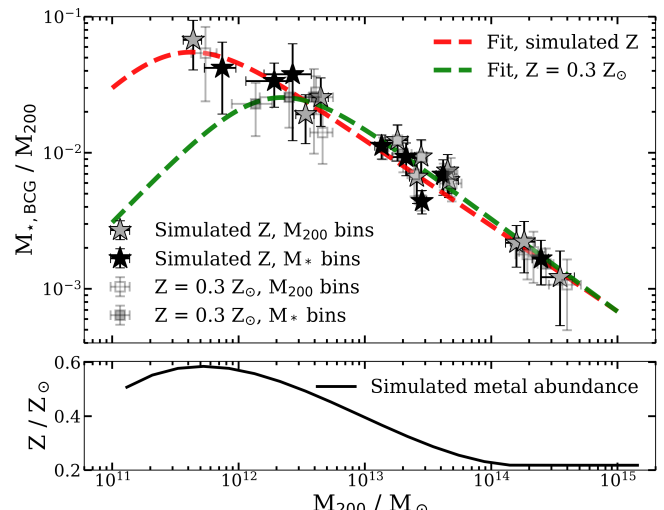


Fig. 3. *Upper panel:* Stellar-to-halo mass ratio as a function of halo mass for different assumptions on the gas metal abundance. Semi-transparent squares show the results of the main analysis, identical to those presented in Figure 2. Star symbols correspond to the same stacked spectra modeled using simulated metal abundances from the lower panel. Dashed lines indicate the best-fitting double powerlaw relations for each case, following Eq. 4. *Lower panel:* Mean gas metal abundance as a function of halo mass derived from the MAGNETICUM simulation and adopted for the spectral modeling shown in the upper panel.

4.4. Comparison with simulations

Figure 4 compares our SHMR measurements with predictions from state-of-the-art hydrodynamical simulations: MAGNETICUM (Dolag et al. 2016, 2025), EAGLE (Crain et al. 2015; Schaye et al. 2015), Illustris (Vogelsberger et al. 2014; Genel et al. 2014; Sijacki et al. 2015), TNG-Cluster (Nelson et al. 2024; Rohr et al. 2024) and different resolution runs of TNG300 and TNG100 (Marinacci et al. 2018; Pillepich et al. 2018; Springel et al. 2018; Naiman et al. 2018; Nelson et al. 2018).

For MAGNETICUM, we used the lightcone covering an area of $30 \times 30 \text{ deg}^2$ out to $z = 0.2$, sampling the local Universe. Galaxy clusters, groups, and their member galaxies were identified using the SubFind halo finder (Springel et al. 2001; Dolag et al. 2009). A detailed description of the lightcone construction is provided in Marini et al. (2025a). SHMRs from Illustris, TNG300, TNG100, and TNG-Cluster were obtained via the public data access of the TNG Project database⁴. For TNG we used snapshot 99, and for Illustris snapshot 135, both corresponding to $z = 0$. The SHMRs are based on precomputed values for central galaxies, where the stellar mass of the brightest central galaxy ($M_{\star, \text{BCG}}$) is measured within twice the stellar half-mass radius. For EAGLE, we used data retrieved from the public EAGLE database⁵. We selected snapshot 27 ($z = 0.10$) from the reference model of the 50 Mpc medium-volume simulation described in Schaye et al. (2015). In this case, the stellar mass of the central galaxy, $M_{\star, \text{BCG}}$, is defined as the total mass of all star particles gravitationally bound to the galaxy. For all the simulations, the halo mass M_{200} is defined as the total mass of the parent dark matter halo enclosed within R_{200} .

There are some major challenges in this kind of comparison. The first lies in the physical implementations in the sim-

⁴ <https://www.tng-project.org/data/>

⁵ <https://eagle.strw.leidenuniv.nl/>

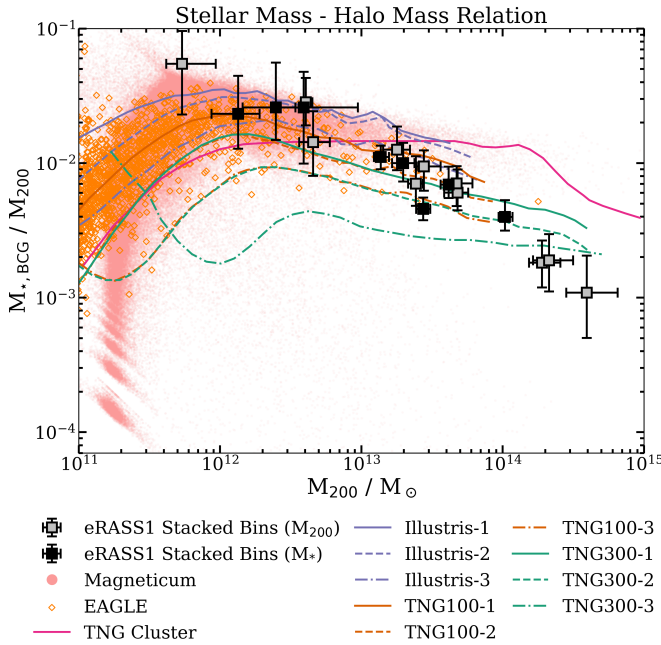


Fig. 4. BCG stellar-to-halo mass ratio as a function of halo mass: comparison with simulations. Black points show stacked results in bins of stellar mass, while grey points show stacked results in bins of halo mass. Colored lines and symbols represent predictions from state-of-the-art hydrodynamical simulations.

ulations themselves. Feedback prescriptions, intracluster light (ICL) formation efficiency, and stellar mass loss can all contribute to differences in the predicted SHMR among different simulations. Another major challenge in this comparison arises from the different methods used to estimate stellar masses for BCGs. In observations, stellar mass is typically measured within an aperture defined by the galaxy's surface brightness profile, often scaled to its effective radius. In simulations we used in this work, the adopted definitions vary: stellar masses may be measured within the stellar half-mass radius or by summing all gravitationally bound star particles. These choices do not necessarily correspond to observational apertures and can lead to systematic offsets, particularly at the high-mass end, where stars associated with the ICL may be partially or fully included in the BCG mass (see Cui et al. 2014, for such an attempt). We believe that these discrepancies can contribute to the significant offsets seen in Figure 4 between the simulations and our observational results.

We find broad agreement near the SHMR knee, albeit with substantial scatter, particularly for the MAGNETICUM, EAGLE, and Illustris simulations. In the halo mass range above $10^{13} M_{\odot}$ and below $10^{14} M_{\odot}$, EAGLE, TNG100, and TNG300-1 simulations show the closest agreement with the data, whereas Illustris and MAGNETICUM tend to slightly overpredict the stellar-to-halo mass ratio. The lower-resolution TNG300-2 and TNG300-3 runs underpredict the ratio across both mass ranges, highlighting the impact of resolution effects. The largest discrepancies occur at the highest halo masses, between 10^{14} and $10^{15} M_{\odot}$. In this regime, only TNG-Cluster and TNG300 provide robust predictions, as simulations with smaller volumes, or for which only a limited-size light-cone was used in this work, do not sample such massive systems. Among these, TNG-Cluster shows the strongest offset, overpredicting the SHMR more significantly than TNG300.

5. Conclusions

We have presented the stellar-to-halo mass relation (SHMR) over the widest halo mass range ($M_{\text{halo}} \sim 10^{12}\text{--}10^{15} M_{\odot}$) ever probed, by using independent estimates of central galaxy stellar masses and host halo masses, derived from eROSITA eRASS1 X-ray data. Our analysis employs the spectral stacking technique described and validated in Toptun et al. (2025) to trace the average X-ray spectra of optically selected groups from the Yang et al. (2007) catalog. Each stacked spectrum was modeled to estimate the hot gas temperature, which was subsequently converted to halo mass via the $M-T_X$ relation of Lovisari et al. (2015).

We find that the SHMR peaks near $M_{200} \sim 10^{12} M_{\odot}$, followed by a decline in the stellar mass fraction toward higher halo masses. This behavior reflects the increasing impact of AGN feedback, which suppresses in-situ star formation, while halo growth proceeds through dark matter accretion and mergers. At these higher masses, the central galaxy builds up its stellar content predominantly via dry mergers. We note that the lowest-mass bins near the peak probe the low-energy sensitivity limit of eROSITA; deeper pointed observations with XMM-Newton (Jansen et al. 2001) and future facilities such as NewAthena (Cruise et al. 2025) will be essential to robustly probe this mass regime.

Our measurements are broadly consistent with previous observational studies based on weak lensing, X-ray analyses of massive clusters, and satellite kinematics, as well as with semi-empirical approaches such as abundance matching and empirical modeling. Comparisons with hydrodynamical simulations reveal discrepancies at the high-mass end, suggesting that current implementations of AGN feedback and star formation efficiency may require further refinement to reproduce the observed SHMR across the full halo mass range.

Finally, the SHMR is known to depend on assembly history and galaxy properties. Variations with BCG morphology, star formation rate, cluster concentration, and BCG-satellite luminosity contrast have been known from the previous studies (Moster et al. 2018; Mandelbaum et al. 2016, 2006; Hudson et al. 2015; Golden-Marx & Miller 2018; Wojtak & Mamon 2013). Future deep, wide-field X-ray surveys such as eRASS:4 will make it possible to extend this analysis to smaller, well-defined subsamples, enabling a more detailed exploration of these secondary dependencies.

Acknowledgements. VT, PP, and IM acknowledge support from the European Research Council (ERC) under the European Union's Horizon Europe research and innovation programme ERC CoG (Grant agreement No. 101045437, PI P. Popesso). KD acknowledges support by the COMPLEX project from the European Research Council (ERC) under the European Union's Horizon 2020 research and innovation program grant agreement ERC-2019-AdG 882679. The calculations for the Magneticum simulations were carried out at the Leibniz Supercomputer Center (LRZ) under the project pr83li. SVZ and VB acknowledge support by the Deutsche Forschungsgemeinschaft, DFG project nr. 415510302. LL acknowledges support from INAF grant 1.05.12.04.01. SE acknowledges financial contribution from the contracts Prin-MUR 2022 supported by Next Generation EU (M4.C2.1.1, n.20227RNLY3 *The concordance cosmological model: stress-tests with galaxy clusters*), and from the European Union's Horizon 2020 Programme under the AHEAD2020 project (grant agreement n. 871158). This research has made use of software provided by the Chandra X-ray Center (CXC) in the application packages CIAO and Sherpa. This work is based on data from eROSITA, the soft X-ray instrument aboard SRG, a joint Russian-German science mission supported by the Russian Space Agency (Roscosmos), in the interests of the Russian Academy of Sciences represented by its Space Research Institute (IKI), and the Deutsches Zentrum für Luft- und Raumfahrt (DLR). The SRG spacecraft was built by Lavochkin Association (NPOL) and its subcontractors, and is operated by NPOL with support from the Max Planck Institute for Extraterrestrial Physics (MPE). The development and construction of the eROSITA X-ray instrument was led by MPE, with contributions from the Dr. Karl Reimann Observatory Bamberg & ECAP (FAU Erlangen-Nuernberg), the University

of Hamburg Observatory, the Leibniz Institute for Astrophysics Potsdam (AIP), and the Institute for Astronomy and Astrophysics of the University of Tübingen, with the support of DLR and the Max Planck Society. The Argelander Institute for Astronomy of the University of Bonn and the Ludwig Maximilians Universität Munich also participated in the science preparation for eROSITA. The eROSITA data shown here were processed using the eSASS software system developed by the German eROSITA consortium. We acknowledge the Virgo Consortium for making their simulation data available. The EAGLE simulations were performed using the DiRAC-2 facility at Durham, managed by the ICC, and the PRACE facility Curie based in France at TGCC, CEA, Bruyères-le-Châtel.

References

Akino, D., Eckert, D., Okabe, N., et al. 2022, *PASJ*, 74, 175

Anders, E. & Grevesse, N. 1989, *Geochim. Cosmochim. Acta*, 53, 197

Baumgartner, W. H., Loewenstein, M., Horner, D. J., & Mushotzky, R. F. 2003, in *AAS/High Energy Astrophysics Division*, Vol. 7, *AAS/High Energy Astrophysics Division #7*, 35.03

Behroozi, P., Wechsler, R. H., Hearin, A. P., & Conroy, C. 2019, *MNRAS*, 488, 3143

Behroozi, P. S., Conroy, C., & Wechsler, R. H. 2010, *ApJ*, 717, 379

Behroozi, P. S., Marchesini, D., Wechsler, R. H., et al. 2013, *ApJ*, 777, L10

Birrer, S., Lilly, S., Amara, A., Paranjape, A., & Refregier, A. 2014, *ApJ*, 793, 12

Burke, D., Laurino, O., wmcLaugh, et al. 2023, *sherpa/sherpa: Sherpa 4.16.0*

Chabrier, G. 2003, *PASP*, 115, 763

Chiu, I., Mohr, J., McDonald, M., et al. 2016, *MNRAS*, 455, 258

Chiu, I.-N., Ghirardini, V., Grandis, S., et al. 2025, *arXiv e-prints*, arXiv:2504.01076

Conroy, C. & Wechsler, R. H. 2009, *ApJ*, 696, 620

Crain, R. A., Schaye, J., Bower, R. G., et al. 2015, *MNRAS*, 450, 1937

Cruise, M., Guainazzi, M., Aird, J., et al. 2025, *Nature Astronomy*, 9, 36

Cui, W., Murante, G., Monaco, P., et al. 2014, *MNRAS*, 437, 816

de Isidó, N. G., Menéndez-Delmestre, K., Gonçalves, T. S., et al. 2024, *ApJ*, 971, 69

DeMaio, T., Gonzalez, A. H., Zabludoff, A., et al. 2018, *MNRAS*, 474, 3009

Diemer, B. 2018, *ApJS*, 239, 35

Dolag, K., Borgani, S., Murante, G., & Springel, V. 2009, *MNRAS*, 399, 497

Dolag, K., Komatsu, E., & Sunyaev, R. 2016, *MNRAS*, 463, 1797

Dolag, K., Remus, R.-S., Valenzuela, L. M., et al. 2025, *A&A*, submitted

Dvornik, A., Hoekstra, H., Kuijken, K., et al. 2020, *A&A*, 642, A83

Eckert, D., Ettori, S., Coupon, J., et al. 2016, *A&A*, 592, A12

Erfanianfar, G., Finoguenov, A., Furnell, K., et al. 2019, *A&A*, 631, A175

Gastaldello, F., Simionescu, A., Mernier, F., et al. 2021, *Universe*, 7, 208

Genel, S., Vogelsberger, M., Springel, V., et al. 2014, *MNRAS*, 445, 175

Ghizzardi, S., Molendi, S., van der Burg, R., et al. 2021, *A&A*, 646, A92

Golden-Marx, J. B. & Miller, C. J. 2018, *ApJ*, 860, 2

Golden-Marx, J. B. & Miller, C. J. 2019, *ApJ*, 878, 14

Golden-Marx, J. B., Miller, C. J., Zhang, Y., et al. 2022, *ApJ*, 928, 28

Gonzalez, A. H., Sivanandam, S., Zabludoff, A. I., & Zaritsky, D. 2013, *ApJ*, 778, 14

Guo, Q., White, S., Li, C., & Boylan-Kolchin, M. 2010, *MNRAS*, 404, 1111

Hansen, S. M., Sheldon, E. S., Wechsler, R. H., & Koester, B. P. 2009, *ApJ*, 699, 1333

Hoekstra, H., Hsieh, B. C., Yee, H. K. C., Lin, H., & Gladders, M. D. 2005, *ApJ*, 635, 73

Hudson, M. J., Gillis, B. R., Coupon, J., et al. 2015, *MNRAS*, 447, 298

Jansen, F., Lumb, D., Altieri, B., et al. 2001, *A&A*, 365, L1

Kravtsov, A. V. & Borgani, S. 2012, *ARA&A*, 50, 353

Kravtsov, A. V., Vikhlinin, A. A., & Meshcheryakov, A. V. 2018, *Astronomy Letters*, 44, 8

Liedahl, D. A., Osterheld, A. L., & Goldstein, W. H. 1995, *ApJ*, 438, L115

Lin, Y.-T. & Mohr, J. J. 2004, *ApJ*, 617, 879

Lovisari, L., Reiprich, T. H., & Schellenberger, G. 2015, *A&A*, 573, A118

Lu, Z., Mo, H. J., Lu, Y., et al. 2015, *MNRAS*, 450, 1604

Mancera Piña, P. E., Read, J. I., Kim, S., et al. 2025, *A&A*, 699, A311

Mandelbaum, R., Seljak, U., Kauffmann, G., Hirata, C. M., & Brinkmann, J. 2006, *MNRAS*, 368, 715

Mandelbaum, R., Wang, W., Zu, Y., et al. 2016, *MNRAS*, 457, 3200

Marinacci, F., Vogelsberger, M., Pakmor, R., et al. 2018, *MNRAS*, 480, 5113

Marini, I., Popesso, P., Dolag, K., et al. 2025a, *A&A*, 694, A207

Marini, I., Popesso, P., Lamer, G., et al. 2024, *A&A*, 689, A7

Marini, I., Popesso, P., Lamer, G., et al. 2025b, *A&A*, 695, C1

Mayes, R. J., Gómez, F. A., & Monachesi, A. 2025, *arXiv e-prints*, arXiv:2506.16645

McNamara, B. R. & Nulsen, P. E. J. 2007, *ARA&A*, 45, 117

Merloni, A., Lamer, G., Liu, T., et al. 2024, *A&A*, 682, A34

Mewe, R., Gronenschild, E. H. B. M., & van den Oord, G. H. J. 1985, *A&AS*, 62, 197

Mewe, R., Lemen, J. R., & van den Oord, G. H. J. 1986, *A&AS*, 65, 511

Montenegro-Taborda, D., Avila-Reese, V., Rodriguez-Gomez, V., Manuwal, A., & Cervantes-Sodi, B. 2025, *MNRAS*, 537, 3954

More, S., van den Bosch, F. C., Cacciato, M., et al. 2011, *MNRAS*, 410, 210

Moster, B. P., Naab, T., & White, S. D. M. 2013, *MNRAS*, 428, 3121

Moster, B. P., Naab, T., & White, S. D. M. 2018, *MNRAS*, 477, 1822

Moster, B. P., Somerville, R. S., Maulbetsch, C., et al. 2010, *ApJ*, 710, 903

Munshi, F., Brooks, A. M., Applebaum, E., et al. 2021, *ApJ*, 923, 35

Naiman, J. P., Pillepich, A., Springel, V., et al. 2018, *MNRAS*, 477, 1206

Nandra, K. & Pounds, K. A. 1994, *MNRAS*, 268, 405

Nelson, D., Pillepich, A., Ayromlou, M., et al. 2024, *A&A*, 686, A157

Nelson, D., Pillepich, A., Springel, V., et al. 2018, *MNRAS*, 475, 624

Pillepich, A., Nelson, D., Hernquist, L., et al. 2018, *MNRAS*, 475, 648

Planck Collaboration, Aghanim, N., Akrami, Y., et al. 2020, *A&A*, 641, A6

Popesso, P., Biviano, A., Bulbul, E., et al. 2024a, *MNRAS*, 527, 895

Popesso, P., Biviano, A., Marini, I., et al. 2024b, *A&A*, submitted, 2411.16555

Popesso, P., Marini, I., Dolag, K., et al. 2025a, *A&A*, 704, A278

Popesso, P., Marini, I., Dolag, K., et al. 2025b, *A&A*, 704, A277

Pratt, G. W., Croston, J. H., Arnaud, M., & Böhringer, H. 2009, *A&A*, 498, 361

Reddick, R. M., Wechsler, R. H., Tinker, J. L., & Behroozi, P. S. 2013, *ApJ*, 771, 30

Reyes, R., Mandelbaum, R., Gunn, J. E., et al. 2012, *MNRAS*, 425, 2610

Robotham, A. S. G., Norberg, P., Driver, S. P., et al. 2011, *MNRAS*, 416, 2640

Rodríguez-Puebla, A., Primack, J. R., Avila-Reese, V., & Faber, S. M. 2017, *MNRAS*, 470, 651

Rohr, E., Pillepich, A., Nelson, D., Ayromlou, M., & Zinger, E. 2024, *A&A*, 686, A86

Salim, S., Lee, J. C., Janowiecki, S., et al. 2016, *ApJS*, 227, 2

Schaye, J., Crain, R. A., Bower, R. G., et al. 2015, *MNRAS*, 446, 521

Shankar, F., Sonnenfeld, A., Mamon, G. A., et al. 2017, *ApJ*, 840, 34

Sijacki, D., Vogelsberger, M., Genel, S., et al. 2015, *MNRAS*, 452, 575

Silk, J. & Rees, M. J. 1998, *A&A*, 331, L1

Springel, V., Pakmor, R., Pillepich, A., et al. 2018, *MNRAS*, 475, 676

Springel, V., White, S. D. M., Tormen, G., & Kauffmann, G. 2001, *MNRAS*, 328, 726

Toptun, V., Popesso, P., Marini, I., et al. 2025, *arXiv e-prints*, arXiv:2505.01502

Urban, O., Werner, N., Allen, S. W., Simionescu, A., & Mantz, A. 2017, *MNRAS*, 470, 4583

van der Burg, R. F. J., Muzzin, A., Hoekstra, H., et al. 2014, *A&A*, 561, A79

van Uitert, E., Cacciato, M., Hoekstra, H., et al. 2016, *MNRAS*, 459, 3251

van Uitert, E., Hoekstra, H., Velander, M., et al. 2011, *A&A*, 534, A14

Vogelsberger, M., Genel, S., Springel, V., et al. 2014, *MNRAS*, 444, 1518

Wang, J., Yang, X., Zhang, J., et al. 2022, *ApJ*, 936, 161

Wang, L., Farrah, D., Oliver, S. J., et al. 2013, *MNRAS*, 431, 648

Wojtak, R. & Mamon, G. A. 2013, *MNRAS*, 428, 2407

Yang, X., Mo, H. J., & van den Bosch, F. C. 2009, *ApJ*, 695, 900

Yang, X., Mo, H. J., van den Bosch, F. C., et al. 2007, *The Astrophysical Journal*, 671, 153, aDS Bibcode: 2007ApJ...671..153Y

Yang, X., Mo, H. J., van den Bosch, F. C., Zhang, Y., & Han, J. 2012, *ApJ*, 752, 41

Zheng, Y.-L., Yang, X., He, M., et al. 2023, *MNRAS*, 523, 4909

Appendix A: Stacked X-ray spectra and spectral modeling results

In this section, we present the stacked X-ray spectra in two different binning schemes and the results of their modeling. Figure A.1 shows the comparison between the X-ray-derived halo masses and the optically based halo mass estimates. Figure A.2 illustrates how the fitted temperature depends on whether the width of the temperature distribution in the GADEM model is fixed or allowed to vary. Figure A.3 shows the stacked spectra for bins based on BCG stellar mass, while Figure A.4 shows the stacked spectra for bins based on optically-derived halo mass from Yang et al. 2007. The spectral modeling results for each bin are provided in Table A.1.

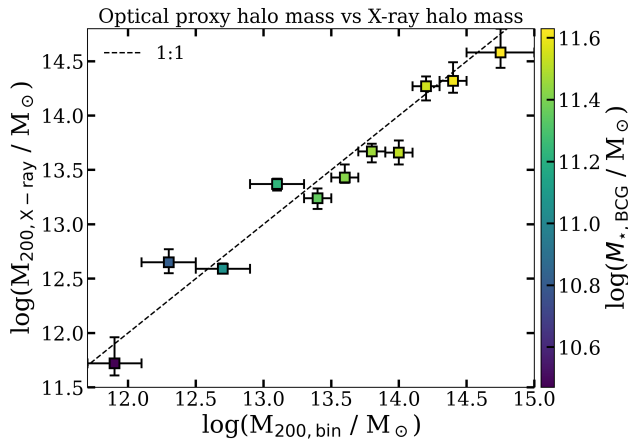


Fig. A.1. X-ray-derived halo mass as a function of the average optically-based halo mass from Yang et al. (2007) for bins of optical halo mass. The color of the points indicates the average stellar mass of the BCG.

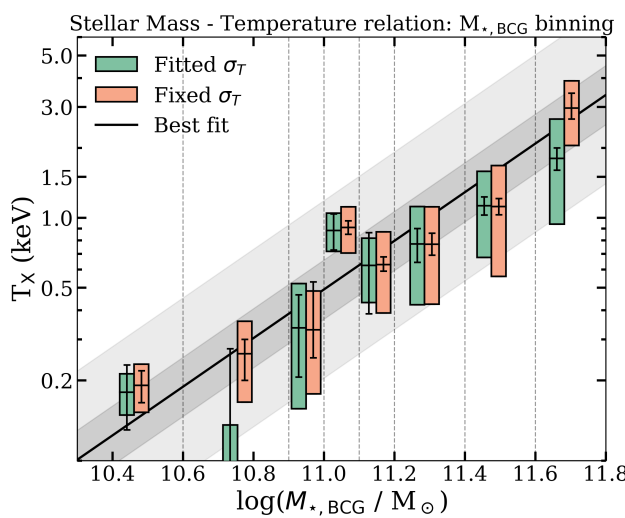


Fig. A.2. Stellar mass-temperature relation for BCGs. Colored boxes show the measured X-ray temperature T_X in each stellar-mass bin; the box center marks the T_X value, while the box height represents the width of the temperature distribution σ_T in the GADEM model. Orange boxes indicate predictions for σ_T and the corresponding T_X obtained from fits with σ_T fixed to these values. Green boxes show results from fits with σ_T left free. The solid line and shaded regions correspond to the best-fit relation from Eq. 2 and its 1σ and 3σ uncertainties. Error bars indicate the uncertainties on T_X for each fitting choice. Vertical lines mark the stellar-mass bin edges; within each bin, all boxes share the same M_* , placed between the boxes.

Table A.1. Spectral modeling results

| $\log_{10}(M_{\text{bin}})$ $M_{\text{bin}} \text{ in } M_\odot$ | kT keV | dof | χ^2 | $\log_{10}(M_{200, \text{xray}})$ $M_{200} \text{ in } M_\odot$ | $\log_{10}(M_*)$ $M_* \text{ in } M_\odot$ |
|---|------------------------|-----|----------|--|---|
| Binning by $M_{200, \text{optical}}$ | | | | | |
| 11.7 – 12.1 | $0.12^{+0.03}_{-0.01}$ | 16 | 1.88 | $11.72^{+0.24}_{-0.11}$ | $10.46^{+0.13}_{-0.14}$ |
| 12.1 – 12.5 | $0.36^{+0.05}_{-0.04}$ | 12 | 2.09 | $12.65^{+0.12}_{-0.10}$ | $10.77^{+0.13}_{-0.13}$ |
| 12.5 – 12.9 | $0.33^{+0.02}_{-0.01}$ | 12 | 1.45 | $12.59^{+0.05}_{-0.04}$ | $11.00^{+0.15}_{-0.12}$ |
| 12.9 – 13.3 | $0.85^{+0.06}_{-0.06}$ | 9 | 1.74 | $13.37^{+0.05}_{-0.06}$ | $11.17^{+0.15}_{-0.11}$ |
| 13.3 – 13.5 | $0.73^{+0.10}_{-0.09}$ | 5 | 1.00 | $13.24^{+0.09}_{-0.10}$ | $11.29^{+0.07}_{-0.06}$ |
| 13.5 – 13.7 | $0.91^{+0.16}_{-0.06}$ | 13 | 1.07 | $13.43^{+0.12}_{-0.05}$ | $11.35^{+0.07}_{-0.06}$ |
| 13.7 – 13.9 | $1.21^{+0.14}_{-0.16}$ | 10 | 1.40 | $13.67^{+0.07}_{-0.10}$ | $11.40^{+0.08}_{-0.06}$ |
| 13.9 – 14.1 | $1.20^{+0.21}_{-0.10}$ | 5 | 1.54 | $13.66^{+0.11}_{-0.06}$ | $11.48^{+0.07}_{-0.06}$ |
| 14.1 – 14.3 | $2.49^{+0.56}_{-0.34}$ | 13 | 1.26 | $14.27^{+0.13}_{-0.09}$ | $11.50^{+0.08}_{-0.05}$ |
| 14.3 – 14.5 | $2.64^{+0.81}_{-0.45}$ | 11 | 0.68 | $14.32^{+0.17}_{-0.11}$ | $11.57^{+0.07}_{-0.06}$ |
| 14.5 – 15.0 | $3.64^{+1.57}_{-0.80}$ | 20 | 1.22 | $14.58^{+0.22}_{-0.14}$ | $11.62^{+0.15}_{-0.10}$ |
| Binning by $M_{*, \text{BCG}}$ | | | | | |
| 10.3 – 10.6 | $0.19^{+0.03}_{-0.03}$ | 16 | 1.12 | $12.12^{+0.15}_{-0.19}$ | $10.46^{+0.09}_{-0.11}$ |
| 10.6 – 10.9 | $0.26^{+0.04}_{-0.06}$ | 19 | 0.91 | $12.38^{+0.14}_{-0.23}$ | $10.75^{+0.10}_{-0.10}$ |
| 10.9 – 11.0 | $0.33^{+0.20}_{-0.08}$ | 7 | 0.96 | $12.58^{+0.38}_{-0.23}$ | $10.95^{+0.03}_{-0.03}$ |
| 11.0 – 11.1 | $0.91^{+0.06}_{-0.06}$ | 7 | 3.06 | $13.43^{+0.05}_{-0.05}$ | $11.05^{+0.03}_{-0.03}$ |
| 11.1 – 11.2 | $0.63^{+0.05}_{-0.04}$ | 10 | 1.92 | $13.12^{+0.06}_{-0.05}$ | $11.15^{+0.03}_{-0.03}$ |
| 11.2 – 11.4 | $0.77^{+0.09}_{-0.08}$ | 16 | 0.99 | $13.28^{+0.08}_{-0.08}$ | $11.29^{+0.07}_{-0.06}$ |
| 11.4 – 11.6 | $1.12^{+0.09}_{-0.09}$ | 12 | 0.86 | $13.61^{+0.05}_{-0.06}$ | $11.48^{+0.08}_{-0.05}$ |
| 11.6 – 11.9 | $2.97^{+0.47}_{-0.31}$ | 17 | 1.36 | $14.42^{+0.09}_{-0.07}$ | $11.68^{+0.08}_{-0.05}$ |

Notes. Results of the spectral stacking and modeling for bins defined by halo mass and BCG stellar mass. For each bin, we report the mass range, the mean gas temperature and its uncertainty derived from bootstrapping of the spectral fit results, the number of degrees of freedom (dof), the reduced χ^2 , the halo mass calculated using the $M-T_X$ relation from Lovisari et al. (2015), and the mean stellar mass in this bin from Salim et al. (2016).

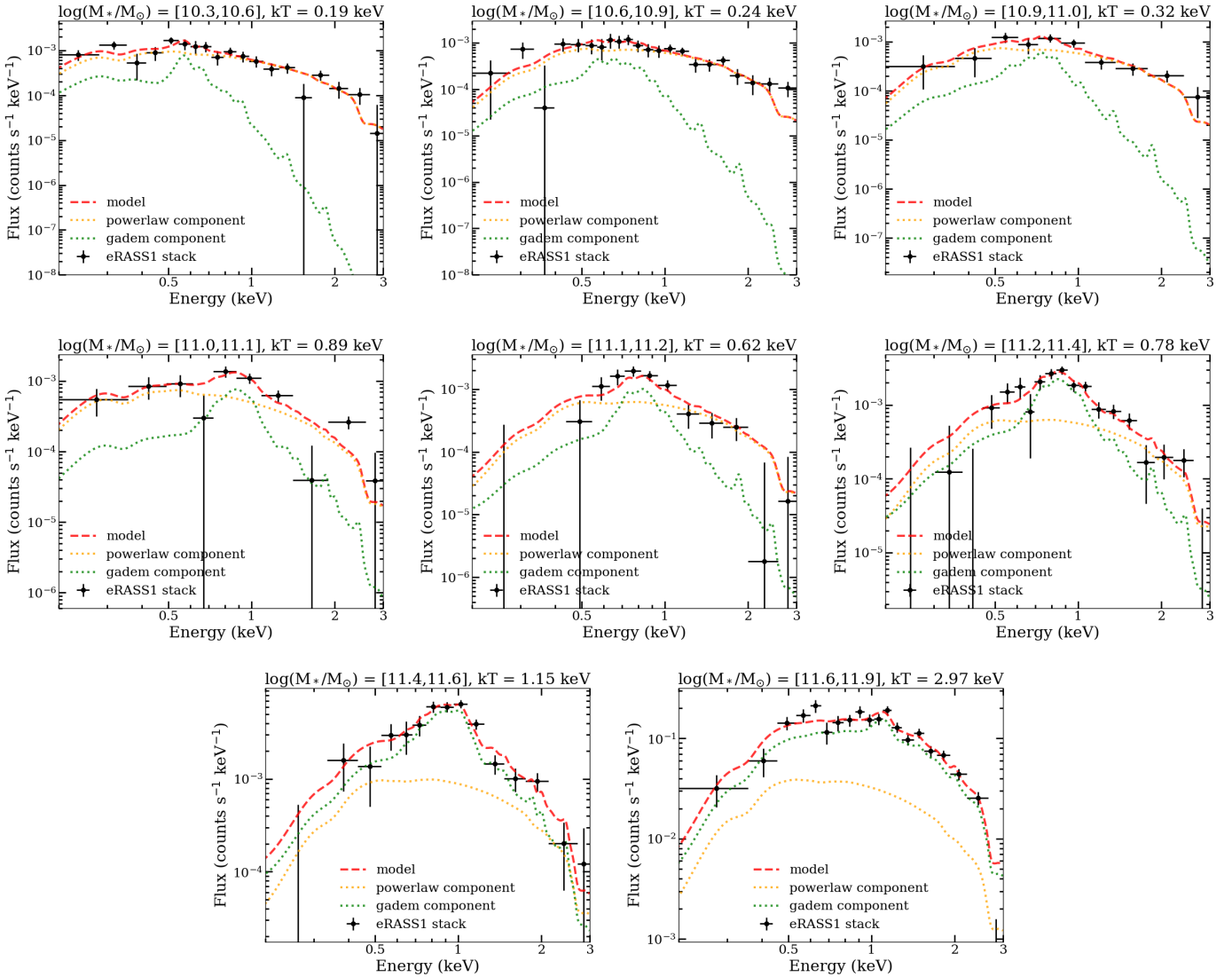


Fig. A.3. Stacked background-subtracted spectra in the 0.2–3 keV energy range for binning by BCG stellar mass. Black points show the observed stacked data, while lines represent the spectral model components: the green line is the ICM emission modeled with GADEM, the yellow line is the power-law component representing unresolved AGN, and the red line is the total model combining all components. The mean temperature of the GADEM component is provided in the title of each panel.

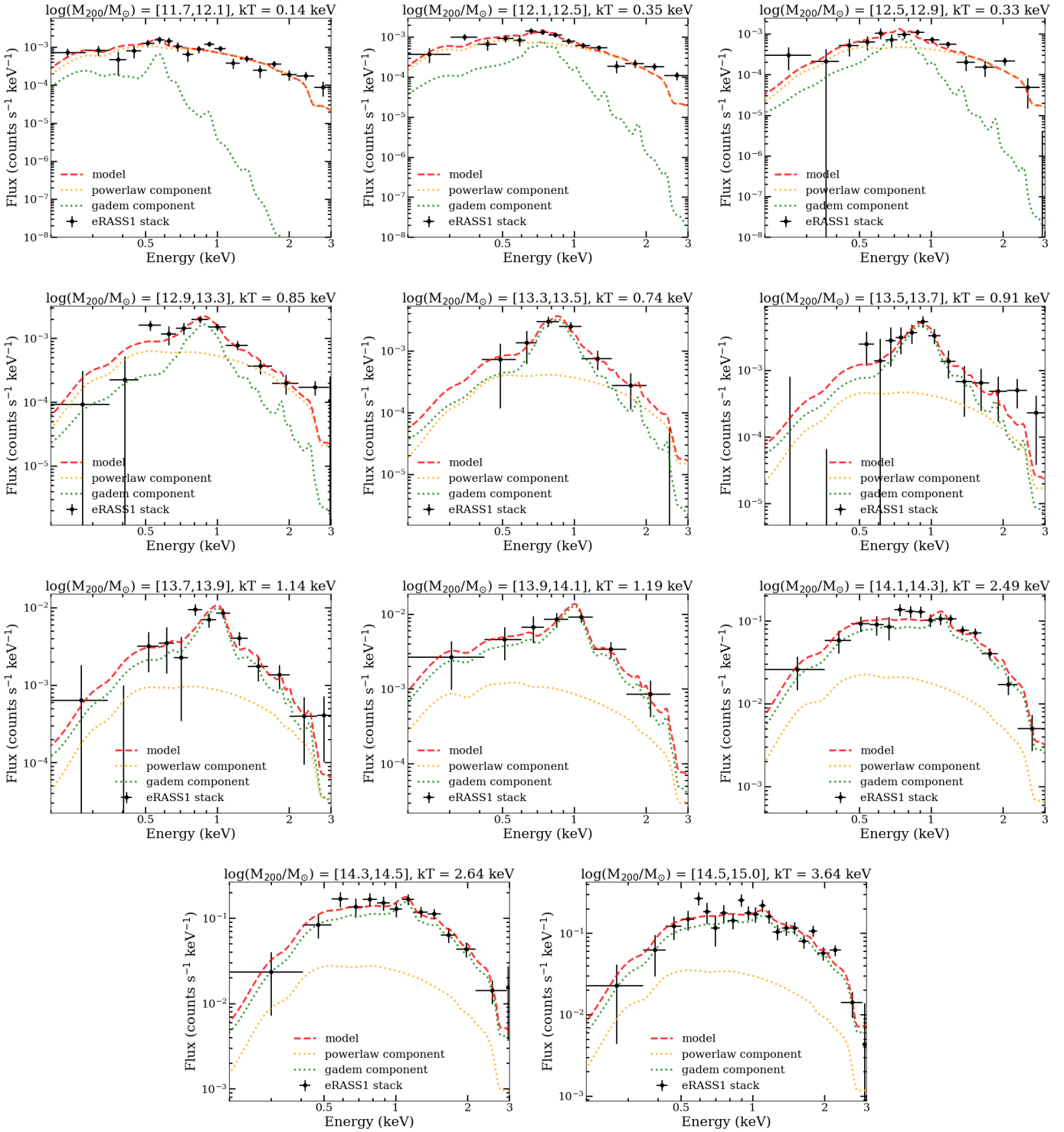


Fig. A.4. Same as A.3 but for the sample binned by halo mass based on characteristic luminosity as described in 2.1.

Appendix B: Validation of stacked temperatures with individual measurements

As a consistency check, we compare the stacked temperature in the highest mass $M_{\star, \text{BCG}}$ bin with the temperatures obtained from individual spectral fits, since in this bin all the sources are bright enough for individual detection. Figure B.1 shows the individual measurements, the stacked result with its 1σ statistical uncertainty, the model width of the temperature distribution σ_T (for more details see Section 2.2 and Figure A.2), and the mean of the individual measurements with its 1σ uncertainty. This comparison demonstrates that the mean of the individual measurements closely matches the stacked temperature, and that the combination of stacking uncertainty and the intrinsic temperature distribution width reproduces the scatter of individual systems, confirming the reliability of the method.

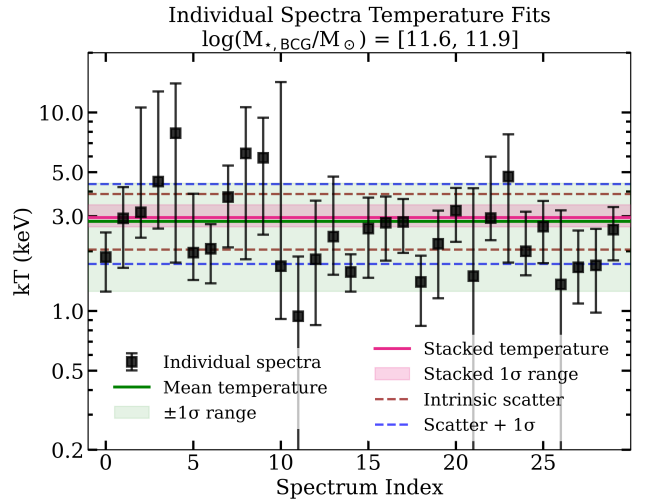


Fig. B.1. Comparison of individual and stacked temperatures in the highest mass $M_{\star, \text{BCG}}$ bin. Datapoints show the temperatures from individual spectral fits with their 1σ errors. The pink solid line and shaded region show the stacked temperature and its 1σ uncertainty from Table A.1. Red dashed lines indicate the model width of the intrinsic temperature distribution σ_T . The green solid line and shaded region correspond to the mean temperature of the individual measurements with its 1σ uncertainty.